High-order wall-resolved large eddy simulation of transonic buffet on the OAT15A airfoil

Will Pazner*,
Lawrence Livermore National Laboratory, Livermore, CA 94550, U.S.A.

Michael Franco† and Per-Olof Persson‡
University of California, Berkeley, Berkeley, CA 94720-3840, U.S.A.

The simulation of the transonic buffet phenomenon caused by shock wave and boundary layer interactions is a challenging problem for standard tools in computational fluid dynamics. We present a numerical study of the OAT15A airfoil at Mach number 0.73, angle of attack 3.5° and Reynolds number 3×10^6. In this work, we make use of a wall-resolved implicit large eddy simulation (WRLES) technique using a high-order discontinuous Galerkin discretization. Without making use of subgrid turbulence models or wall models, the WRLES simulation successfully predicts transonic buffet at an angle of attack of 3.5°. This method results in good agreement with computational results obtained using detached eddy simulation (DES) method, and fair agreement with experimental results. We study the effect of mesh refinement, polynomial degree, and artificial viscosity parameters on the accuracy of the distribution of the pressure coefficient on the upper surface of the airfoil, and compare both 2D and 3D simulations.

I. Introduction

Transonic flow over an airfoil can result in complex interactions between shock waves and the viscous boundary layer. A particularly interesting and challenging phenomenon is that of transonic buffet, whereby the flow separation induces instabilities, unsteady behavior and structural vibrations, termed buffeting.[8,33] This strong phenomenon can cause dangerous vibrations leading to the destruction of a wing or a turbomachine blade.[17] The origin and onset of transonic buffet has been studied experimentally,[17,19] in the context of global stability theory,[11,12] and computationally, using a variety of discretizations and approaches.[6,7,15]

The numerical simulation of transonic buffet on airfoils[18] is highly challenging, due to its unsteady nature, the turbulent flows, and the complex interaction between shocks and flow separation.[13] Most of the

*Sidney Fernbach Postdoctoral Fellow, Center for Applied Scientific Computing, Lawrence Livermore National Laboratory, Livermore, CA 94550. E-mail: pazner1@llnl.gov. AIAA Member.

†Ph.D. Student, Department of Mathematics, University of California, Berkeley, Berkeley CA 94720-3840. E-mail: michaelfranco@berkeley.edu. AIAA Student Member.

‡Associate Professor, Department of Mathematics, University of California, Berkeley, Berkeley CA 94720-3840. E-mail: persson@berkeley.edu. AIAA Senior Member.

This work was performed under the auspices of the U.S. Department of Energy by Lawrence Livermore National Laboratory under Contract DE-AC52-07NA27344. This document was prepared as an account of work sponsored by an agency of the United States government. Neither the United States government nor Lawrence Livermore National Security, LLC, nor any of their employees makes any warranty, expressed or implied, or assumes any legal liability or responsibility for the accuracy, completeness, or usefulness of any information, apparatus, product, or process disclosed, or represents that its use would not infringe privately owned rights. Reference herein to any specific commercial product, process, or service by trade name, trademark, manufacturer, or otherwise does not necessarily constitute or imply its endorsement, recommendation, or favoring by the United States government or Lawrence Livermore National Security, LLC. The views and opinions of authors expressed herein do not necessarily state or reflect those of the United States government or Lawrence Livermore National Security, LLC, and shall not be used for advertising or product endorsement purposes. This material is also based upon work supported by the National Science Foundation Graduate Research Fellowship Program under Grant No. DGE 1752814. Any opinions, findings, and conclusions or recommendations expressed in this material are those of the authors and do not necessarily reflect the views of the National Science Foundation.

standard tools in computational fluid dynamics for modeling turbulence are based on the unsteady Reynolds-averaged Navier-Stokes (URANS) equations, which are widely believed to produce unreliable results for massively separated unsteady flows.[4,29] Alternative approaches such as large eddy simulation (LES) and hybrid methods such as detached eddy simulation (DES)[30] are typically better at modeling these flow problems, however at several magnitudes higher computational cost.

During the last decade, higher order accurate discretizations such as the discontinuous Galerkin (DG) method[10] have been shown to be highly efficient for LES simulations.[3,26,31] In particular, the so-called implicit LES (ILES) method which uses the natural dissipation from the numerical scheme as a subgrid closure model, has been used successfully for a range of model problems.[32] These simulations are usually performed on grids that resolve the boundary layer in the normal direction, but have significant stretching in the streamwise and the spanwise directions to reduce the total number of elements. This regime is often referred to as wall-resolved LES (WRLES), as opposed to wall-modeled LES (WMLES) methods which use various techniques to model the flow in the boundary layer and somehow couple to the LES solver further away from the flow.[5,22]

In this work, we apply a state-of-the-art high-order DG solver to the simulation of transonic buffet on the ONERA OAT15A airfoil. This is a well-studied model problem with many experimental[17] and numerical[13,15] results to compare with. Our main focus is to evaluate our high-order methods for modeling this phenomenon, in particular with respect to (a) the numerical stability of the solvers and the high-order approximations, and (b) the accuracy of the resulting flow predictions. A fundamental difficulty with high-order methods is the treatment and stabilization of shocks and other under-resolved features of the solution. Here, we use the artificial visocisty approach developed in Refs. 27, 28, which achieves subgrid resolution using a highly sensitive indicator based on orthogonal polynomials.

II. Governing equations and discretization

The governing equations are the compressible Navier-Stokes equations in d spatial dimensions, stabilized by adding a Laplacian diffusion term to each equation. We solve these equations in terms of the conservative variables $\boldsymbol{u} = (\rho, \rho\boldsymbol{v}, \rho E)$, where ρ is the density, $\boldsymbol{v} \in \mathbb{R}^d$ is the velocity, and E is the total energy per unit mass. We write the system in conservation form:

$$\frac{\partial \boldsymbol{u}}{\partial t} + \nabla \cdot \left(\boldsymbol{F}^I(\boldsymbol{u}) + \boldsymbol{F}^V(\boldsymbol{u}, \nabla \boldsymbol{u}) - \varepsilon \nabla \boldsymbol{u} \right) = 0, \tag{1}$$

where the F^I and F^V are the inviscid and viscous flux functions, respectively. F^I is given by the Euler fluxes,

$$\boldsymbol{F}^I(\boldsymbol{u}) = \begin{pmatrix} \rho\boldsymbol{v} \\ \rho\boldsymbol{v} \otimes \boldsymbol{v}^T + pI \\ \rho H \boldsymbol{v} \end{pmatrix}, \tag{2}$$

and the viscous flux is defined by

$$\boldsymbol{F}^V = \begin{pmatrix} 0 \\ -\boldsymbol{\tau} \\ q_j - v_i \tau_{ij} \end{pmatrix}, \tag{3}$$

where I is the $d \times d$ identity matrix, p is the pressure, $H = E + p/\rho$ is the stagnation enthalpy, and the viscous stress tensor $\boldsymbol{\tau}$ and heat flux $\boldsymbol{q}$ are defined by

$$\tau_{ij} = \mu \left(\frac{\partial v_i}{\partial x_j} + \frac{\partial v_j}{\partial x_i} - \frac{2}{3} \frac{\partial v_k}{\partial x_k} \delta_{ij} \right), \qquad q_j = -\frac{\mu}{\mathrm{Pr}} \frac{\partial}{\partial x_j} \left(E + \frac{p}{\rho} - \frac{1}{2} v_k v_k \right). \tag{4}$$

Here μ is the coefficient of viscosity defined in terms of the Reynolds number Re, and Pr is the Prandtl number, which we take to be $\mathrm{Pr} = 0.72$. The system is closed by the equation of state

$$p = (\gamma - 1)\rho \left(E - \|\boldsymbol{v}\|^2/2 \right). \tag{5}$$

The parameter ε controls the artificial viscosity required for shock capturing. The definition of ε is of great importance in this work, and will be discussed in detail below.

A. Discontinuous Galerkin discretization

For the spatial discretization we use a standard nodal discontinuous Galerkin method. The physical domain Ω is discretized using a high-order mesh $\mathcal{T}_h$ consisting of curved elements K_i mapped from the tensor-product reference element $[0,1]^d$ using an isoparametric mapping denoted T_i. Test and trial functions are drawn from the finite element function space

$$V_h = \{v : \Omega \to \mathbb{R} : v|_{K_i} \in V_h(K_i) \text{ for each element } K_i \in \mathcal{T}_h\}\,. \tag{6}$$

The local isoparametric function space is defined by

$$V_h(K_i) = \left\{v : K_i \to \mathbb{R} : v(\boldsymbol{x}) = q\left(T_i^{-1}(\boldsymbol{x})\right) \text{ for some } q \in \mathcal{Q}^p\left([0,1]^d\right)\right\}, \tag{7}$$

where $\mathcal{Q}^p$ is the space of all polynomials of degree at most p in each variable, defined by

$$\mathcal{Q}^p\left([0,1]^d\right) = \left\{ q : [0,1]^d \to \mathbb{R} : q(\boldsymbol{x}) = \sum_{\boldsymbol{\beta}} c_{\boldsymbol{\beta}} \boldsymbol{x}^{\boldsymbol{\beta}}, \beta_j \leq p \right\}, \tag{8}$$

where $\boldsymbol{\beta}$ is a multi-index.

The viscous fluxes and Laplacian term are formulated using the CDG method.[25] As in the local discontinuous Galerkin (LDG) method,[9] these fluxes include a parameter C_{11} that plays the role of a penalization or stabilization term, similar to that of an interior penalty or Nitsche method.[1,2,20] The CDG method allows for setting the C_{11} parameter to be identically zero. However, in this work we use the value defined on each element by $C_{11} = 20/h_{\min}$ where $h_{\min}$ is the height of the element, in order to provide additional nonlinear stabilization. At the domain boundary, we impose the boundary conditions weakly through an appropriate choice of numerical fluxes.

B. Stabilization by artificial viscosity

A defining feature of the transonic flows that are the subject of this work is the shock wave that induces the buffet phenomenon. However, shocks and discontinuities in the flow field can result in spurious oscillations that degrade the quality of the solution and potentially result in negative density or pressure, thus halting the simulation. In order to capture these sharp features while damping the oscillations, we make use of an artificial viscosity field based on a resolution sensor.

The main idea behind the resolution sensor is to determine the decay rate of the expansion coefficients of the solution in an orthogonal basis. For smooth solutions, the coefficients in the expansion are expected to decay very quickly. But when the solution is under-resolved, the strength of the discontinuity will dictate the rate of decay of the expansion coefficients. Our resolution sensor is based on the amount of the highest order coefficients for one of the solution components, within each element.

We first expand the solution within each element in terms of a hierarchical family of orthogonal polynomials. Therefore, we write a scalar solution component u in terms of the orthogonal basis functions ψ_i as

$$u = \sum_{i=1}^{N_p} u_i \psi_i, \tag{9}$$

where N_p is the dimension of the solution space. In all of our examples we choose the density ρ as the scalar field, which in our experience results in a highly sensitive yet selective shock indicator. We express the solution of order p within each element in terms of an orthogonal basis, consider a truncated expansion of the same solution, and define a resolution indicator as:

$$u = \sum_{i=1}^{N_p} u_i \psi_i, \qquad \hat{u} = \sum_{i=1}^{N_{p-1}} u_i \psi_i, \qquad S_e = \log_{10}\left(\frac{(u-\hat{u}, u-\hat{u})_e}{(u,u)_e}\right)$$

Next we determine an element-wise viscosity ε_e over each element e by the following function,

$$\varepsilon_e = \begin{cases} 0 & \text{if} \quad s_e < s_0 - \kappa\ , \\ \frac{\varepsilon_0}{2}\left(1 + \sin\frac{\pi(s_e - s_0)}{2\kappa}\right) & \text{if} \quad s_0 - \kappa \leq s_e \leq s_0 + \kappa\ , \\ \varepsilon_0 & \text{if} \quad s_e > s_0 + \kappa\ . \end{cases} \tag{10}$$

Here, $s_e = \log_{10} S_e$ and the parameters $\varepsilon_0 \sim h/p$, $s_0 \sim 1/p^4$, and κ are chosen empirically sufficiently large so as to obtain a sharp but smooth shock profile.[27,28] ε_0 determines the strength of the viscosity, and s_0 controls the selectivity the viscosity indicator function. These element-wise viscosities are used to define a piecewise-constant field $\varepsilon(\boldsymbol{x}) = \varepsilon_{K(\boldsymbol{x})}$, where $K(\boldsymbol{x})$ identifies the element to which $\boldsymbol{x}$ belongs.

To reduce the amount of numerical artifacts due to the piecewise nature of this indicator, we form a new continuous viscosity field $\varepsilon_0(\boldsymbol{x}) \in C^0(\Omega)$. This viscosity field is formed by assigning to each mesh vertex the maximum viscosity value among all neighboring elements K. These values are then interpolated linearly within each element.

Since the viscosity fields depend on the solution in a non-local way, the Jacobian matrix has a wider stencil than the original DG scheme and it is difficult to compute. However, for time-accurate solutions we have found that it is sufficient to weakly couple the sensor to the Navier-Stokes equations. More specifically, for our implicit Runge-Kutta time integrator we simply compute a viscosity field at each initial time and make use of this time-lagged viscosity for the entire timestep. This simplifies the nonlinear solvers significantly, since the solution-dependency of the sensor does not have to be considered in the Jacobian matrices.

C. Semi-discrete equations and temporal integration

The spatial discretization leads to a semi-discrete form:

$$\boldsymbol{M}\frac{d\boldsymbol{U}}{dt} = \boldsymbol{R}(\boldsymbol{U}), \tag{11}$$

for solution vector $\boldsymbol{U}$, mass matrix $\boldsymbol{M}$, and residual function $\boldsymbol{R}(\boldsymbol{U})$. We integrate this system of ordinary differential equations in time using an efficient, stage-parallel, fully implicit, Radau IIA Runge-Kutta method[24] with analytical Jacobian matrices and a block-ILU(0) preconditioned GMRES solver. The use of a fully implicit Runge-Kutta method for the temporal integration allows for the solution of the temporal stages in parallel, thereby reducing the number of mesh partitions, and improving the strong scaling of the solver.

D. Problem configuration

The spatial domain is taken to be the rectangle $[-50, 100] \times [-50, 50]$ with the leading edge of the OAT15A airfoil placed at the origin. The chord length is normalized to be 1. Thus, all domain boundaries are at least 50 chord lengths from the airfoil, and the wake region has a length of 100 chord lengths. Far-field conditions are enforced at domain boundaries, and a no-slip wall condition is enforced at the surface of the airfoil. The freestream velocity is chosen in accordance with the angle of attack $\alpha = 3.5°$. The Mach number is $M = 0.73$ and the Reynolds number based on the chord length is $\mathrm{Re} = 3 \times 10^6$. For the three-dimensional simulations, the domain is extruded 0.2 chord-lengths in the spanwise direction, and periodic boundary conditions are enforced at the plane of symmetry.

We consider a sequence of four two-dimensional meshes, each increasing in resolution. All of the meshes used are unstructured quadrilateral meshes with areas of refinement located in the boundary layer, the trailing edge of the airfoil, and the shock location on the upper surface of the airfoil. The boundary layer elements are generated through a sequence of 8 to 10 structured refinements in the transverse direction, resulting in highly anisotropic elements, with aspect ratios of up to approximately 1000:1. In order to perform the wall-resolved large eddy simulation, we require that $y^+ < 1$ for the entire length of the boundary layer. We note that for this problem, $y^+ = 1$ corresponds to a distance of about 8.45×10^{-6} units from the surface of the airfoil. The coarsest mesh we use has a boundary layer element thickness of approximately 2.32×10^{-6} units and the finest mesh has a boundary layer element thickness of about 7.25×10^{-7} units. Moreover, the use of high-degree polynomials results in a smaller effective y^+. These small and highly stretched elements give rise to an extremely restrictive CFL stability condition that necessitates the use of implicit time integration. The four meshes (denoted I, II, III, and IV) are shown in Figure 1. We used Mesh II and Mesh III as a basis for the 3D simulations. The 2D meshes were extruded in the spanwise direction, such that each quadrilateral element results in 20 hexahedral elements, giving rise to a total of 163,720 hexahedra for Mesh II and 286,600 hexahedra for Mesh III. For both 3D simulations, we use quadratic $p = 2$ polynomials, resulting in 4,420,440 nodes, or 22,102,200 total degrees of freedom for Mesh II, and 7,738,200 nodes, corresponding to a total of 38,691,000 degrees of freedom for Mesh III.

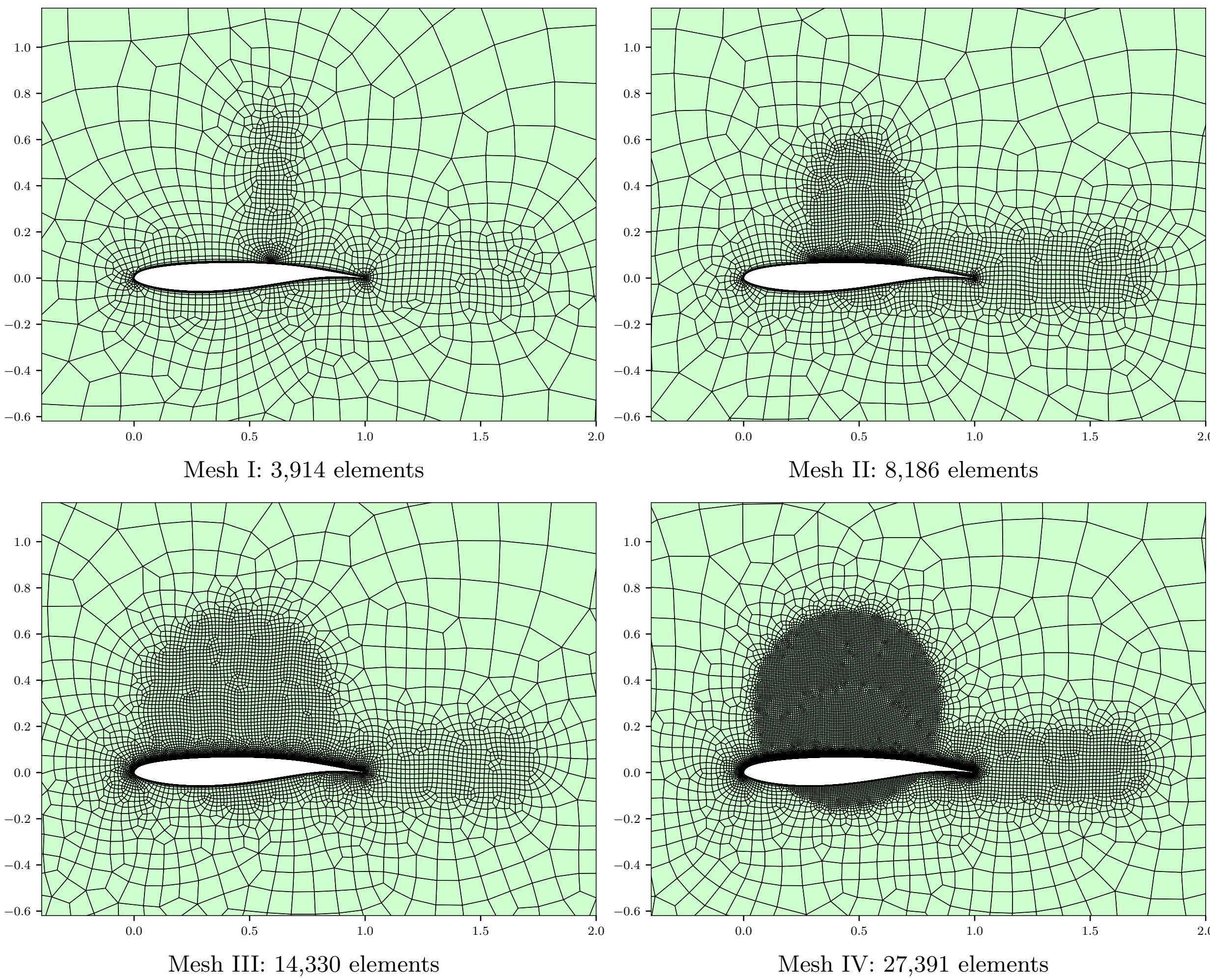

Figure 1: Sequence of two-dimensional meshes used in this study (showing zoom-in around the airfoil).

III. Results and analysis

A. 2D results

We begin by performing a sequence of simulations on the 2D meshes shown in Figure 1. We additionally vary discretization parameters such as polynomial degree p and viscosity threshold s_0. We summarize the simulation configurations in Table 1. The viscosity threshold s_0 is chosen experimentally in order to minimize the effect of the viscosity while still maintaining stability. For all but the coarsest mesh used, we observe the buffet phenomenon and shock oscillation.

Table 1: 2D simulation configurations and comparison with literature

Study	Parameters	Shock oscillation
Mesh I	$p = 2, s_0 = -5.0$	✗
Mesh II	$p = 2, s_0 = -4.3$	✓
	$p = 3, s_0 = -4.5$	✓
	$p = 4, s_0 = -5.5$	✓
Mesh III	$p = 2, s_0 = -4.3$	✓
Mesh IV	$p = 2, s_0 = -3.8$	✓
URANS[6]	$\alpha = 3.5°$	✗
	$\alpha = 4.0°$	✓
IDDES[15]	10.2×10^6 DOFs/comp.	✓

1. *Mesh I*

This mesh is the coarsest mesh used in this study, consisting of only 3,914 quadrilateral elements. Unstructured mesh refinement was performed in a narrow band above the surface of the airfoil in order to sharply resolve the initial shock location. In this simulation, we did not observe the buffet or shock oscillation, likely due to under-resolution of the shock region immediately above the airfoil. Additionally, the observed shock location was too far downstream when comparing with experimental and computational reference data. The shock location was observed to be steady at around 0.5 chord lengths. These results are generally consistent with those of Ref. 6, where no shock oscillation was observed using a URANS method. Our conclusion for this test case is that Mesh I is too coarse in order to adequately resolve the small-scale features required for an accurate LES simulation. In Figure 2 we show a snapshot of the pressure and artificial viscosity obtained using this mesh, and compare with the results obtained on Mesh III.

2. *Mesh II*

In order to address the under-resolution observed in the previous test case, we created Mesh II by further refining the mesh around the surface of the airfoil and in the wake. We also expanded the region of refinement around the shock location above the airfoil. This refined mesh consists of slightly more than twice as many quadrilateral elements as Mesh I. This mesh was used for a sequence of three 2D simulations, using $p = 2$, $p = 3$, and $p = 4$, in order to study the effect of polynomial degree on the accuracy of the results. In all simulations, we observe the buffet phenomenon and shock oscillation. In Figure 3 we display several snapshots of the pressure field computed on this mesh, illustrating the buffet phenomenon. We also compute the coefficient of pressure on the surface of the airfoil, as well as mean pressure fluctuations. The coefficient of pressure is displayed in Figure 4. Using $p = 2$, we observe good agreement with the previous computational results of Huang and colleagues,[15] which made use of an improved delayed detached eddy simulation (IDDES) method. The resolution sensor is chosen using the parameter $s_0 = -4.3$. The shock location is predicted to be slightly further upstream than what is observed in experiments, and the pressure coefficient appears to plateau after the initial shock location (an effect not present in experimental data). Using $p = 3$ and $p = 4$ polynomials, we obtain a more accurate prediction of the initial shock location, and better agreement

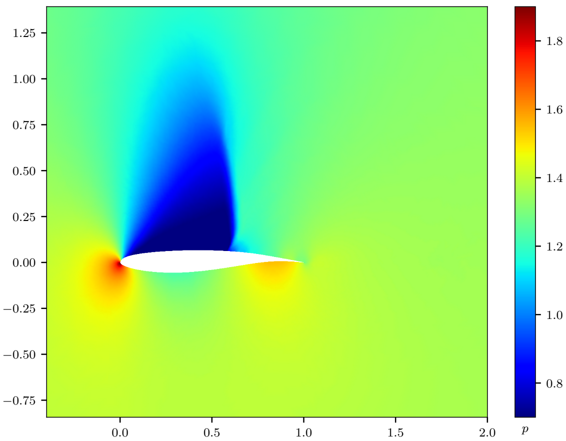

Snapshot of pressure on Mesh I. We note the shock location is stationary, and too far downstream when compared with experimental data, likely due to mesh under-resolution.

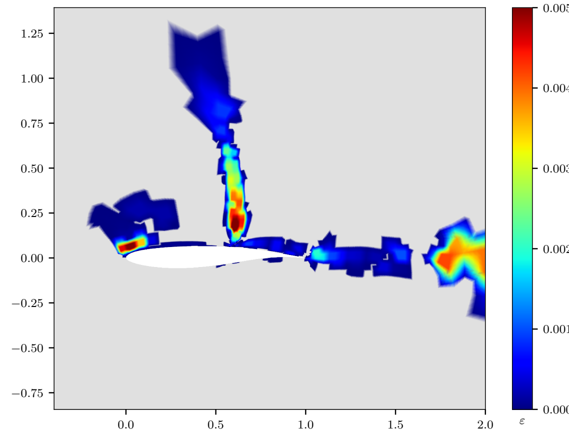

Artificial viscosity field on Mesh I. Grey background indicates regions in which no viscosity is added. The sensor is mostly active in the vicinity of the shock, but also in the boundary layer and wake regions.

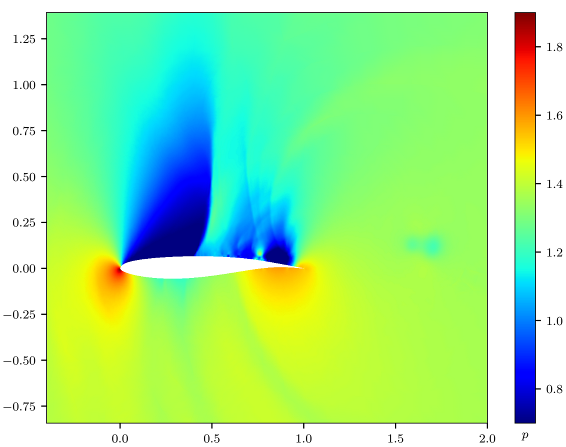

Snapshot of pressure on Mesh III. The shock location is further upstream in comparison to the results obtained on Mesh I.

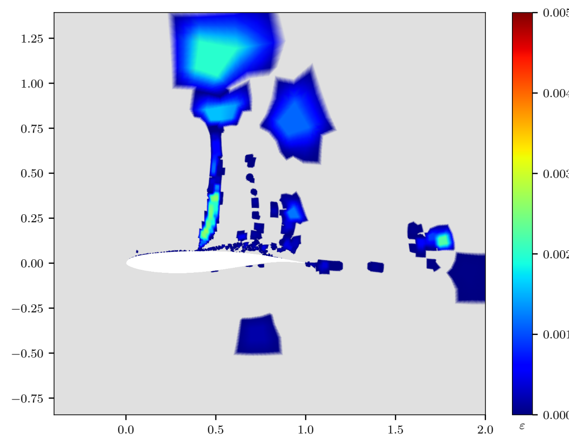

Artificial viscosity field on Mesh III. When comparing with the results obtained on Mesh I, we see that the viscosity coefficient is significantly smaller, and the sensor is less active in the boundary layer and towards the leading edge of the airfoil.

Figure 2: Comparison of pressure (left) and artificial viscosity fields (right) obtained using Mesh I (top) and Mesh III (bottom). Mesh I is under-resolved, resulting in a downstream shock location and strong artificial viscosity field required for stabilization. In comparison, the shock location obtained using Mesh III is more accurate, and the artificial viscosity is smaller and more selective.

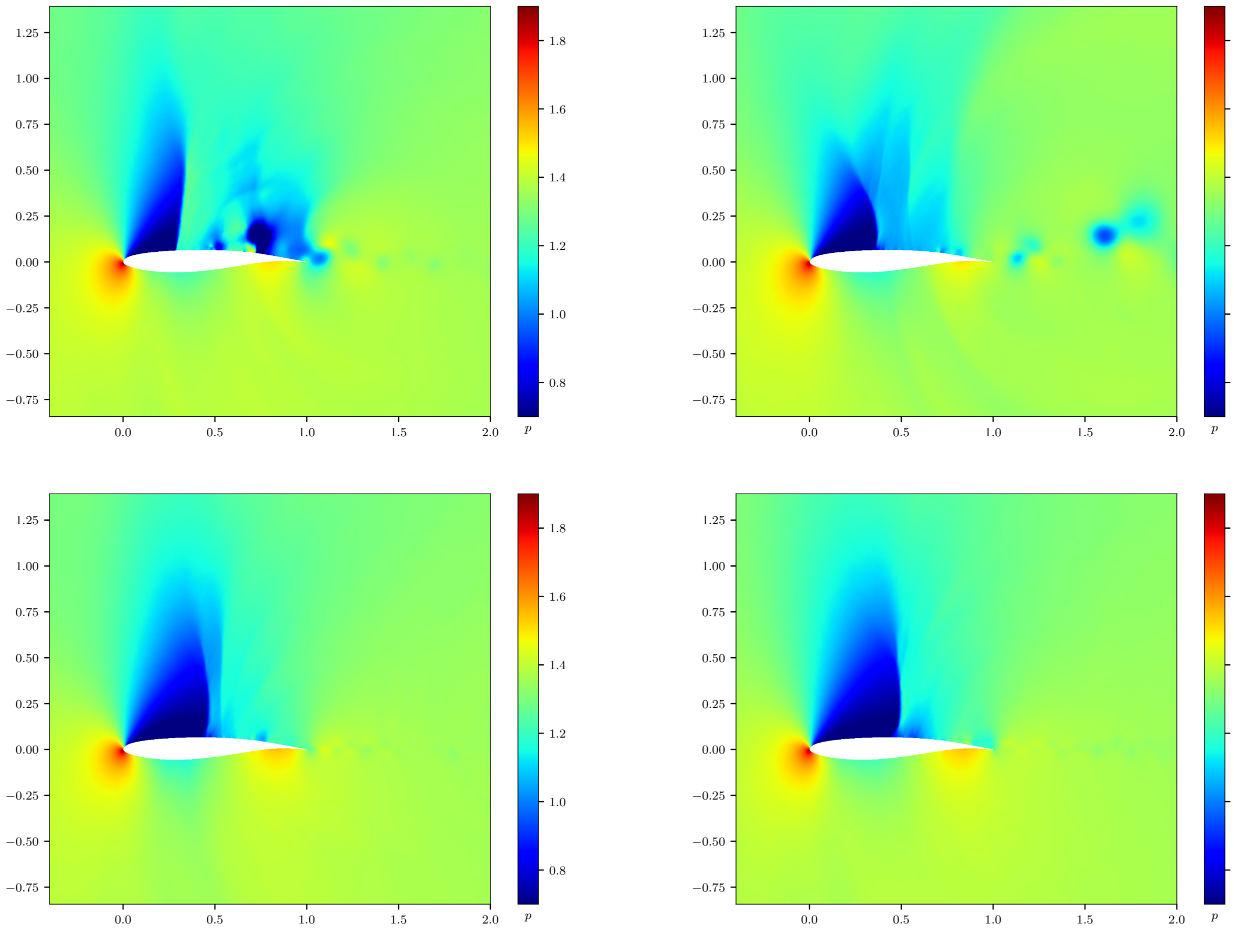

Figure 3: Snapshots of pressure computed using Mesh II with $p = 2$, showing oscillation of the shock location.

with experimental data towards the trailing edge. Because the use of higher degree polynomials can result in larger oscillations near discontinuities, for the $p = 4$ case we choose less selective shock sensors with $s_0 = -5.5$ for this case. However, our results also include a secondary, weaker shock downstream of the first shock. We believe this downstream shock is likely a numerical artifact, either due to the oscillatory nature of the high-degree polynomials or our treatment of artificial viscosity. In Figure 4 we also present the mean pressure fluctuations on the surface of the airfoil. The results for $p = 3$ and $p = 4$ were very similar, and so we present only the $p = 4$ case below. Our results are largely consistent with experiment and numerical results; however, we do observe larger fluctuations towards the trailing edge of the airfoil. We hypothesize that this is partly because of the secondary shock, and partly because we average over a relatively small number of flow cycles.

3. Mesh III and Mesh IV

Mesh III is obtained by further expanding the area of refinement above the surface of the airfoil, such that the region or refinement spans almost the entire length of the airfoil. Mesh IV is a variant of Mesh III, where the mesh size field is chosen to be smaller within the regions of refinement. We run the simulation on both of these meshes using $p = 2$. The artificial viscosity threshold is set to $s_0 = -4.3$ for Mesh III and $s_0 = -3.8$ for Mesh IV, as this was experimentally determined to result in a stable simulation with minimal degradation of solution quality. The coefficient of pressure obtained using Mesh III closely matches the experimental data, and the RMS pressure fluctuations agree well with experimental data in the vicinity of the shock, but deviate further downstream. One explanation for this deviation from experimental data is the presence of a weaker secondary shock downstream from the first shock, which is likely caused by numerical effects. The coefficient of pressure and pressure fluctuations obtained using Mesh IV closely matches that obtained using

Mesh II with $p = 4$. The initial shock location is well predicted by the simulations using Mesh II with $p = 4$, Mesh III, and Mesh IV, suggesting that these configurations are sufficiently resolved.

B. 3D results

We generate two 3D hexahedral meshes by extruding Mesh II and Mesh III by 0.2 chord lengths in the y-direction, obtaining meshes with 163,360 and 286,600 isoparametric hexahedral elements, respectively. We run both simulations with $p = 2$, resulting in a total of 22,102,200 and 38,691,000 degrees of freedom. The meshes are partitioned into 1680 partitions and run in parallel on 60 Broadwell nodes of NASA's Pleaides supercomputer. In Figure 5, we show several snapshots of the solution, visualized using isosurfaces of the Q-criterion,[14,16] $Q = -\frac{1}{2} v_{i,j} v_{j,i}$, colored by velocity magnitude. The shock location is shown as a $M = 1$ isosurface, and the oscillatory shock motion is illustrated over approximately one half-period. We compute the time- and spanwise-averaged coefficient of pressure at the surface of the airfoil and present the results in Figure 4. Although some differences are expected to be observed between the 2D and 3D buffet phenomenon,[21] the main flow features remain largely similar between the 2D and 3D simulations. This observation is consistent with other results from the literature.[17]

The 3D simulations do not exhibit the secondary, spurious shock that is present in some of our 2D simulations, indicating that perhaps this feature is an artifact of the 2D discretization. As a result, the downstream results for both the coefficient of pressure and mean pressure fluctuations much more closely match the experimental data. The 3D mesh based on Mesh II results in a shock location that is too far upstream, and more limited shock oscillation. However, when we use the extruded version of Mesh III, which is further refined around the shock location and in the boundary layer, we recover a more accurate shock location and larger shock motion, giving results that more closely match the reference data.

C. Robustness and solver performance

This work has allowed us to study the robustness of high-order DG methods when applied to a challenging test case with many complex features. The approach of using wall-resolved LES for a problem with Reynolds number 3×10^6 results in extremely small, anisotropic boundary layer elements, which can prove challenging for discretizations and solvers. Additionally, the main focus of this study is the ability of these methods to accurately capture the transonic buffet phenomenon, which arises as the result of a complex interaction between transonic shocks, viscous boundary layer effects, and upstream moving waves from the trailing edge. Thus, it is of great importance to stabilize the shocks while ensuring that sufficiently little artificial dissipation is added, allowing the method to properly resolve these small-scale features.

The extremely small boundary layer elements necessitate the use of implicit time integration schemes, and correspondingly, robust linear and nonlinear solvers to efficiently solve the resulting systems. In this work, we made use of fully implicit Radau IIA Runge-Kutta methods, using stage-uncoupled block ILU(0) preconditioners.[24] These methods have successfully been applied to lower Mach number LES problems in 2D and 3D,[23] but this study further demonstrates their utility when applied to transonic flow problems. For all of the simulations performed in this study, we were able to use a time-accurate time step of $\Delta t = 10^{-3}$, which is several magnitudes larger than the largest allowable explicit time step, especially on the refined meshes.

In this study, we have found that the parameters that have the greatest influence on the stability and robustness of the method are those concerning the artificial viscosity. If the viscosity is chosen to be too selective by taking s_0 to be too large, then the solution can develop oscillations in the vicinity of the shock, leading to negative density or pressure. Empirical evidence suggests that the stability is relatively insensitive to the parameter κ in (10), which we have taken to be 1 in all of the runs performed in this work. Although scaling arguments can be used to determine roughly how s_0 and ε_0 should scale in terms of h and p, these arguments do not result in explicit expressions for these values, and experience suggests that the proper values are highly mesh- and problem-dependent. We have also found that the spatial order p of the numerical method has little effect on the shock capturing and stability of the solution.

IV. Conclusions

In this work we have performed a series of 2D and 3D simulations of transonic buffet on the ONERA OAT15A airfoil at $\mathrm{Re} = 3 \times 10^6$ and $\alpha = 3.5^\circ$ using a wall-resolved LES methodology. Using a very

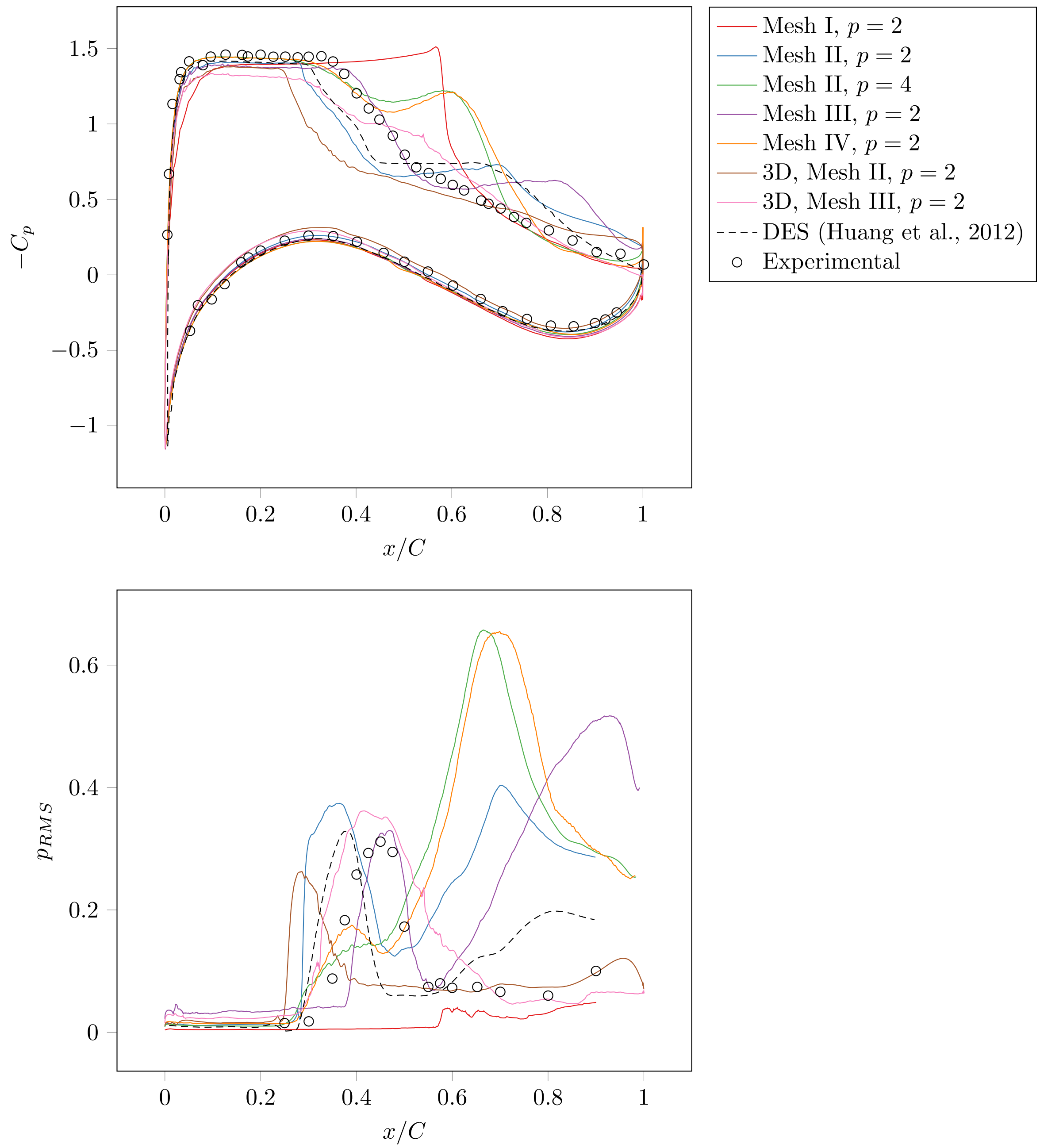

Figure 4: Left: coefficient of pressure for the OAT15A airfoil using simulation configurations listed in Table 1. Right: RMS pressure fluctuations on the suction side of the airfoil for the same configurations.

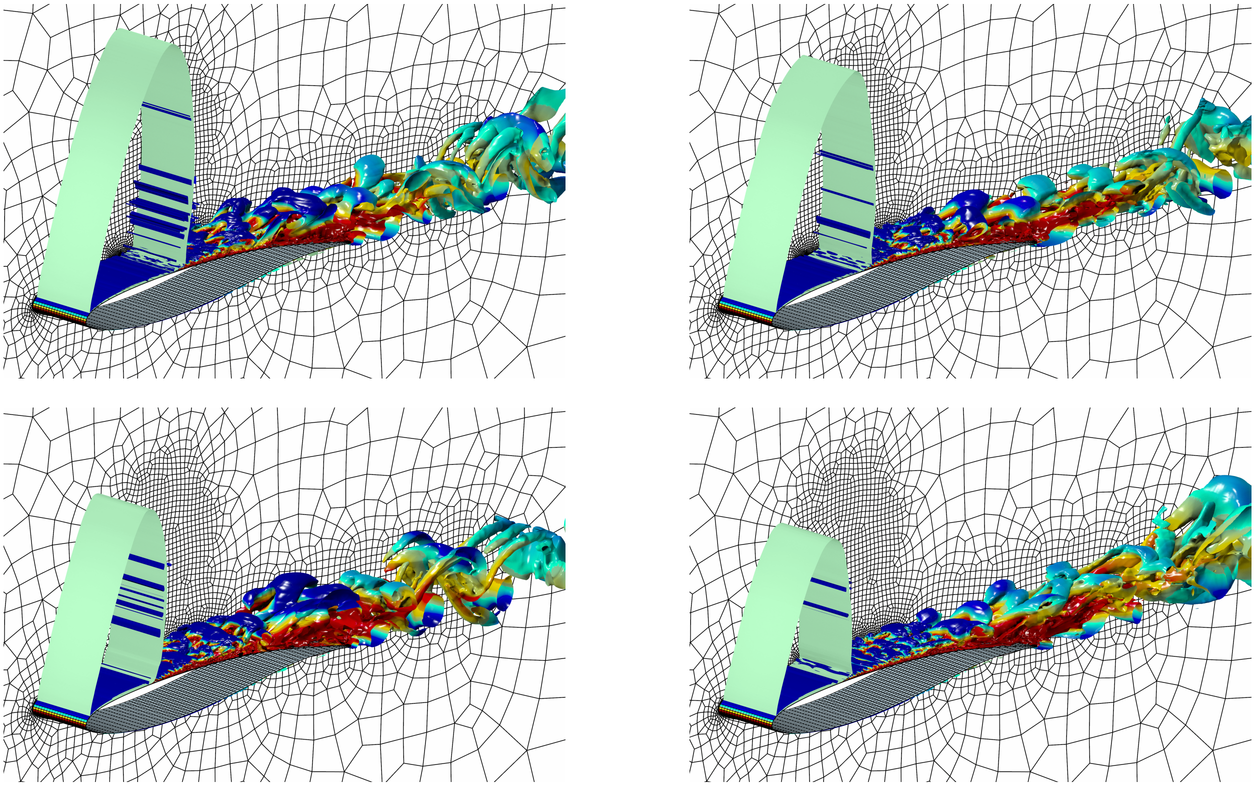

Figure 5: Snapshots of 3D solution, showing isosurfaces of Q-criterion, colored by velocity magnitude. The location of the shock is visualized in green using a Mach 1 isosurface.

coarse and under-resolved mesh, we obtain results similar to URANS,[6,7] where no shock oscillation was observed. By refining the mesh in the vicinity of the shock, we are able to predict the shock oscillation, obtaining results largely consistent with previous DES computational studies.[15] Further mesh refinements and increasing the polynomial degree result in better agreement with experimental data for the initial shock location. Our two-dimensional results differ from experimental data for the coefficient of pressure and RMS pressure fluctuations downstream from the shock. This difference is largely due to a spurious secondary shock, which we hypothesize is an artifact of the 2D discretization. Our three-dimensional results do not exhibit this behavior, and thus give much more accurate results in the downstream region. This work has also allowed us to study the robustness of fully implicit Runge-Kutta methods applied to transonic problems using an artificial viscosity approach for shock capturing. Overall we observed that the implicit solvers perform well, and the artificial viscosity approach results in a stable discretization while also resolving the shock location. The solution remained stable when solving the problem with a wide range of mesh and discretization parameters. The iterative solvers converged rapidly even when applied to the large-scale problems. However, the choice of parameters for the shock capturing resolution sensor seems to have a significant effect on the solution quality, and so the development of a methodology for the automatic selection of these parameters would be an interesting topic for future development.

V. Acknowledgements

This work was performed under the auspices of the U.S. Department of Energy by Lawrence Livermore National Laboratory under Contract DE-AC52-07NA27344. This work was also supported by the National Aeronautics and Space Administration (NASA) under grant number NNX16AP15A. M.F. was supported by the National Science Foundation Graduate Research Fellowship Program under Grant No. DGE 1752814.

References

[1]D. N. Arnold. An interior penalty finite element method with discontinuous elements. *SIAM Journal on Numerical Analysis*, 19(4):742–760, August 1982.

[2]D. N. Arnold, F. Brezzi, B. Cockburn, and L. D. Marini. Unified analysis of discontinuous Galerkin methods for elliptic problems. *SIAM Journal on Numerical Analysis*, 39(5):1749–1779, January 2002.

[3]A. D. Beck, T. Bolemann, D. Flad, H. Frank, G. J. Gassner, F. Hindenlang, and C.-D. Munz. High-order discontinuous galerkin spectral element methods for transitional and turbulent flow simulations. *International Journal for Numerical Methods in Fluids*, 76(8):522–548, August 2014.

[4]J. Bodart, J. Larsson, and P. Moin. Large eddy simulation of high-lift devices. In *21st AIAA Computational Fluid Dynamics Conference*. American Institute of Aeronautics and Astronautics, June 2013.

[5]S. T. Bose and G. I. Park. Wall-modeled large-eddy simulation for complex turbulent flows. *Annual Review of Fluid Mechanics*, 50(1):535–561, January 2018.

[6]V. Brunet. Computational study of buffet phenomenon with unsteady RANS equations. In *21st AIAA Applied Aerodynamics Conference*. American Institute of Aeronautics and Astronautics, June 2003.

[7]V. Brunet, S. Deck, P. Molton, and M. Thiery. A complete experimental and numerical study of the buffet phenomenon over the OAT15A airfoil. In *40ème Colloque Aérodynamique Appliquèe*, 2005.

[8]D. Caruana, A. Mignosi, M. Corrège, A. Le Pourhiet, and A.M. Rodde. Buffet and buffeting control in transonic flow. *Aerospace Science and Technology*, 9(7):605–616, October 2005.

[9]B. Cockburn and C.-W. Shu. The local discontinuous Galerkin method for time-dependent convection-diffusion systems. *SIAM Journal on Numerical Analysis*, 35(6):2440–2463, December 1998.

[10]B. Cockburn and C.-W. Shu. Runge–Kutta discontinuous Galerkin methods for convection-dominated problems. *Journal of Scientific Computing*, 16(3):173–261, 2001.

[11]J. D. Crouch, A. Garbaruk, D. Magidov, and A. Travin. Origin of transonic buffet on aerofoils. *Journal of Fluid Mechanics*, 628:357, June 2009.

[12]J.D. Crouch, A. Garbaruk, and D. Magidov. Predicting the onset of flow unsteadiness based on global instability. *Journal of Computational Physics*, 224(2):924–940, June 2007.

[13]S. Deck. Numerical simulation of transonic buffet over a supercritical airfoil. *AIAA Journal*, 43(7):1556–1566, July 2005.

[14]Y. Dubief and F. Delcayre. On coherent-vortex identification in turbulence. *Journal of Turbulence*, 1:N11, January 2000.

[15]J. Huang, Z. Xiao, J. Liu, and S. Fu. Numerical investigation of shock buffet on an OAT15A airfoil and control effects of vortex generators. In *50th AIAA Aerospace Sciences Meeting including the New Horizons Forum and Aerospace Exposition*. American Institute of Aeronautics and Astronautics, January 2012.

[16]J. C. R. Hunt, A. A. Wray, and P. Moin. Eddies, streams, and convergence zones in turbulent flows. Technical Report CTR-S88, Center for Turbulence Research, 1988.

[17]L. Jacquin, P. Molton, S. Deck, B. Maury, and D. Soulevant. Experimental study of shock oscillation over a transonic supercritical profile. *AIAA Journal*, 47(9):1985–1994, September 2009.

[18]B. H. K. Lee. Oscillatory shock motion caused by transonic shock boundary-layer interaction. *AIAA Journal*, 28(5):942–944, May 1990.

[19]J. B. McDevitt and A. F. Okuno. Static and dynamic pressure measurements on a NACA 0012 airfoil in the Ames high Reynolds number facility. Technical Report 19850019511, NASA Ames Research Center, 1985.

[20]J. Nitsche. Über ein Variationsprinzip zur lösung von Dirichlet-Problemen bei Verwendung von Teilräumen, die keinen Randbedingungen unterworfen sind. *Abhandlungen aus dem Mathematischen Seminar der Universität Hamburg*, 36(1):9–15, July 1971.

[21]E. Paladini, J. Dandois, D. Sipp, and J.-Ch. Robinet. Analysis and comparison of transonic buffet phenomenon over several three-dimensional wings. *AIAA Journal*, pages 1–18, October 2018.

[22]G. I. Park. Wall-modeled large-eddy simulation of a high Reynolds number separating and reattaching flow. *AIAA Journal*, 55(11):3709–3721, November 2017.

[23]W. Pazner. *Efficient solvers and preconditioners for the implicit time integration of discontinuous Galerkin methods*. PhD thesis, Brown University, 2018.

[24]W. Pazner and P.-O. Persson. Stage-parallel fully implicit Runge–Kutta solvers for discontinuous Galerkin fluid simulations. *Journal of Computational Physics*, 335:700–717, April 2017.

[25]J. Peraire and P.-O. Persson. The compact discontinuous Galerkin (CDG) method for elliptic problems. *SIAM Journal on Scientific Computing*, 30(4):1806–1824, January 2008.

[26]J. Peraire and P.-O. Persson. High-order discontinuous Galerkin methods for CFD. In *Advances in Computational Fluid Dynamics*, pages 119–152. World Scientific, March 2011.

[27]P.-O. Persson. Shock capturing for high-order discontinuous Galerkin simulation of transient flow problems. In *21st AIAA Computational Fluid Dynamics Conference*. American Institute of Aeronautics and Astronautics, June 2013.

[28]P.-O. Persson and J. Peraire. Sub-cell shock capturing for discontinuous Galerkin methods. In *44th AIAA Aerospace Sciences Meeting and Exhibit*. American Institute of Aeronautics and Astronautics, January 2006.

[29]W. Rodi. Comparison of LES and RANS calculations of the flow around bluff bodies. *Journal of Wind Engineering and Industrial Aerodynamics*, 69-71:55–75, July 1997.

[30]P. R. Spalart, S. Deck, M. L. Shur, K. D. Squires, M. Kh. Strelets, and A. Travin. A new version of detached-eddy simulation, resistant to ambiguous grid densities. *Theoretical and Computational Fluid Dynamics*, 20(3):181–195, May 2006.

[31]A. Uranga, P.-O. Persson, M. Drela, and J. Peraire. Implicit large eddy simulation of transitional flows over airfoils and wings. In *19th AIAA Computational Fluid Dynamics*. American Institute of Aeronautics and Astronautics, June 2009.

[32] A. Uranga, P.-O. Persson, M. Drela, and J. Peraire. Implicit large eddy simulation of transition to turbulence at low Reynolds numbers using a discontinuous Galerkin method. *International Journal for Numerical Methods in Engineering*, 87(1-5):232–261, October 2010.

[33] C. J. Wood. Transonic buffeting on aerofoils. *Journal of the Royal Aeronautical Society*, 64(599):683–686, November 1960.